Scientific Research Publishing

Advances in Aerospace Science and Technology, 2026, 11(2), 58-76
https://www.scirp.org/journal/aast
ISSN Online: 2473-6724
ISSN Print: 2473-6708

Aerodynamic Interference and Trajectory Analysis of Sub-UAV Separation from a Composite-Wing Aircraft

Hao He, Qi Wang*

Department of Aeronautics and Astronautics, Nanchang Hangkong University, Nanchang, China
Email: *wangqi439@126.com

How to cite this paper: He, H. and Wang, Q. (2026) Aerodynamic Interference and Trajectory Analysis of Sub-UAV Separation from a Composite-Wing Aircraft. *Advances in Aerospace Science and Technology*, **11**, 58-76.
https://doi.org/10.4236/aast.2026.112004

Received: March 17, 2026
Accepted: April 19, 2026
Published: April 22, 2026

Copyright © 2026 by author(s) and Scientific Research Publishing Inc.
This work is licensed under the Creative Commons Attribution International License (CC BY 4.0).
http://creativecommons.org/licenses/by/4.0/

Open Access

Abstract

This paper uses the Unsteady Reynolds-Averaged Navier-Stokes (URANS) method, sliding/overset mesh technique and coupled 6-degree-of-freedom (6-DOF) dynamic model to study sub-UAV deployment from a composite-wing carrier in cruise and hover conditions. After validating the numerical framework via a hovering rotor case and a benchmark store separation case, it compares the performance of inboard/outboard deployment positions and different deployment strategies, and develops a quasi-steady spatial distortion envelope bounded by actuator saturation limits to provide a theoretical basis for safe hardpoint layout. The results show that aerodynamic interference at the outboard deployment position in hover is significantly stronger (by approximately 43%) due to rotor wake asymmetry, and confirm that the accelerated gravity-drop strategy is safer than the traditional tube launch method.

Keywords

Aerodynamic Interference, UAV Deployment, Flight Trajectory, Separation Strategies, CFD

1. Introduction

The deployment of sub-UAVs from composite-wing VTOL launch platforms during hover introduces severe aerodynamic challenges. Unlike fixed-wing store separation [1]-[4], VTOL release subjects the sub-UAV to intense rotor downwash, asymmetric slipstreams, and highly nonlinear shear layers. Rotor–wake coupling can rapidly saturate control surfaces beyond actuator limits—causing attitude divergence or mid-air collision [5]. Extant studies focus on store separation from fixed-wing jets and conventional helicopters [6] [7]. There are three key chal-

lenges hinder safe low-speed separation for composite-wing VTOL systems:

First of all is that the Safe separation boundaries rarely account for actuator limits (e.g., max pitch/yaw moments) when assessing aerodynamic compatibility [7]. The next one is the oversimplified models: The Momentum Source Method (MSM) smears discrete tip vortices [8] [9] and fails to capture "aerodynamic lag" during shear-layer penetration—masking critical high-frequency vortex–body interactions [10]. Then is the unvalidated strategies: It remains unclear whether traditional catapults [11] or accelerated gravity-drop [12] better ensure dynamic compatibility in slipstream flow.

To address these, this study employs high-fidelity URANS and polyhedral overset mesh techniques [13] to dynamically simulate the composite-wing UAV separation process. The principal contributions are threefold. First, we quantitatively correlate the rotor cant angle and local vorticity with sub-UAV control authority degradation. Second, we formulate a spatial distortion envelope strictly governed by actuator saturation limits, providing a theoretical baseline for safe hardpoint positioning. Finally, dynamic trajectory validation demonstrates that an accelerated gravity-drop strategy fundamentally outperforms traditional tube launches; by rapidly penetrating the highly sheared rotor wake, it minimizes interference residence time and effectively prevents attitude divergence.

2. Geometric Model and Numerical Methods

2.1. Geometric Model and Mesh Generation Methods

This study investigates the rotor downwash effects during the initial deployment of a tandem-wing sub-UAV from a composite-wing carrier. To reduce computational cost, the carrier was simplified to its core fuselage-wing-rotor geometry. Concurrently, the folded tandem-wings sub-UAV was modeled as a hemispherical-nosed cylinder (900 mm long, 120 mm diameter), providing the physical slender-body basis for the Covert separation criterion. Key system parameters and spatial meshes are detailed in **Table 1** and **Figure 1**, respectively.

Table 1. Parameters of the composite-wing carrier and sub-UAV system.

Parameters	value
Rotor geometry (inch)	NS62 × 24
Hovering rotational speed (rpm)	3600
Rotor inboard tilt angle (˚)	3
Forward rotor hub center[a] (x, y, z) (m)	(0.655, 1.45, 0)
Rear rotor hub center[a] (x, y, z) (m)	(3.455, 1.45, 0)
Carrier aircraft wingspan (m)	6.5
Mass of Sub-UAV (kg)	6
Length of Sub-UAV (m)	0.9

Continued

Tail moment arm (m)	0.64
Wing area of Sub-UAV per Wing (m^2)	0.096
Sub-UAV center of gravity location[a] (x, y, z) (m)	(2.055, 0, −0.02)
Sub-UAV Moment of inertia, I (kg·m^2)	(0.08, 0.396, 0.396)

a. All geometric dimensions and spatial coordinates are referenced to the nose of the Carrier aircraft.

To accurately capture the unsteady flow fields during separation while accommodating the disparate kinematics of the carrier's rotors and the sub-UAV, a hybrid meshing strategy was adopted. The sub-UAV separation was simulated using the dynamic overset grid technique, by executing dynamic hole-cutting and boundary interpolation.

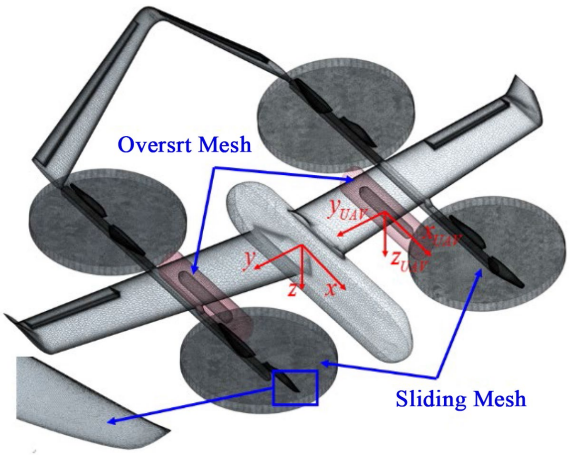

Figure 1. Calculation model and Grid diagram (Simplified model).

Additionally, the sliding mesh technique was utilized for the high-speed propeller rotation with a sliding interface establishing to physically update cell angular positions at each time step.

2.2. CFD Methodology

The unsteady Reynolds-averaged Navier-Stokes (URANS) equations were discretized using a finite volume method (FVM) on unstructured polyhedral grids. For an arbitrary control volume, the three-dimensional integral form of the governing equations is expressed as:

$$\frac{\partial}{\partial t}\iiint_{\Omega} W\mathrm{d}V + \iint_{\partial\Omega} F(W)n\mathrm{d}S = \iint_{\partial\Omega} G(W)n\mathrm{d}S \tag{1}$$

In Equation (1), V and S denote the control volume and its boundary; is the conserved variable vector, $F(W)$ and $G(W)$ are the inviscid and viscous fluxes, and is the outward unit normal vector. The Shear Stress Transport (SST)

$k-\omega$ turbulence model was employed to resolve the severe adverse pressure gradients and flow separation induced by multi-body interference. The governing equations were discretized using a second-order upwind scheme spatially and a dual-time stepping method temporally to ensure unsteady accuracy.

To resolve the viscous sublayer without employing empirical wall functions, the near-wall spatial resolution was strictly constrained to ensure a non-dimensional wall distance of $y^+ \approx 1$ across all critical aerodynamic surfaces. The flow information across the sliding and overset interfaces was dynamically updated using a distance-weighted interpolation method.

2.3. Numerical Modeling of Flight Dynamics

By integrating the aerodynamic forces and moments obtained from the unsteady flow field, the rigid-body six-degree-of-freedom (6-DOF) equations of motion were established. The transient kinematic parameters, including translational velocities, spatial displacements, and angular rates, were determined by numerically solving these coupled equations.

$$\left.\begin{aligned} F_x &= m\left(\dot{u}+wq-vr\right) \\ F_y &= m\left(\dot{v}+ur-wp\right) \\ F_z &= m\left(\dot{w}+vp-uq\right) \\ \bar{L} &= \dot{p}I_{xx}+\left(I_{zz}-I_{yy}\right)rq \\ M &= \dot{q}I_{yy}+\left(I_{xx}-I_{zz}\right)pr \\ N &= \dot{r}I_{zz}+\left(I_{xx}-I_{yy}\right)pq \end{aligned}\right\} \tag{2}$$

$$\left.\begin{aligned} \dot{x} &= V\cos\mu\cos\varphi \\ \dot{y} &= V\cos\mu\sin\varphi \\ \dot{z} &= -V\sin\mu \\ \dot{\phi} &= p+\tan\theta\left(q\sin\phi+r\cos\phi\right) \\ \dot{\theta} &= q\cos\phi-r\sin\phi \\ \dot{\psi} &= \frac{q\sin\phi+r\cos\phi}{\cos\theta} \end{aligned}\right\} \tag{3}$$

In Equation (2) and Equation (3), m is the sub-UAV mass; F_x, F_y, F_z and $\bar{L}, M, N$ are the resultant forces and aerodynamic moments along the body axes; u, v, w and p, q, r denote the translational and angular velocities, respectively. I_{xx}, I_{yy}, I_{zz} are the principal moments of inertia (products of inertia are neglected due to geometric symmetry). Additionally, x, y, z represent the inertial coordinates, V is the airspeed, and μ and φ define the flight path and heading angles. The vehicle attitude is defined by the Euler angles ϕ, θ, ψ, whose rates ($\dot{\phi}, \dot{\theta}, \dot{\psi}$) are nonlinearly coupled with p, q, r via standard kinematic transformations.

3. Method Validation and Grid Independence

3.1. Mesh Generation and Grid Independence Study

The computational domain was discretized using an unstructured mesh with local refinements on critical aerodynamic surfaces. To resolve the boundary layer, 31 prism layers were applied with a first-layer height of 1.61×10^{-5} m and a 1.2 growth rate. Furthermore, cylindrical refinement zones were established around the propellers to capture high-gradient rotational flows. Figure 2 illustrates the resulting computational domain and surface grids.

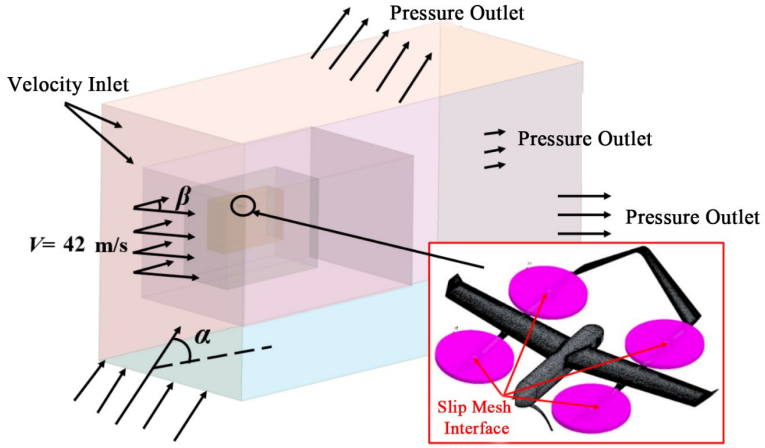

Figure 2. Grid diagram of the system.

For the fixed-wing cruise validations and subsequent separation analysis, the far-field boundaries were defined as velocity inlets and pressure outlets under standard atmospheric conditions, with the freestream velocity initialized at 42 m/s, angle of attack 0˚, propeller speed 0 rpm. To ensure spatial convergence, a grid independence study evaluated five mesh resolutions (3.5 to 17.5 million cells) using the mated carrier-sub configuration in steady level flight. As detailed in Table 2, the lift and drag coefficients (C_L, C_D) exhibited asymptotic convergence. Because the relative deviations became negligible (<1%) beyond 13.57 million cells, this resolution was adopted for all unsteady simulations to optimally balance physical fidelity and computational cost.

Table 2. Grid independence verification.

Number of grids (Millions)	Lift of system (kN)	Drag of aircraft (kN)
3.72	2.966	0.2345
6.75	3.022	0.2368
10.02	3.024	0.2372
13.57	3.026	0.2364
17.03	3.027	0.2366

3.2. Validation of Rotor Aerodynamics and Sliding Mesh Technique

To validate the sliding mesh flow solver, the dynamic pressure distribution of an isolated hovering rotor [14] was simulated. As illustrated in Figure 3, dynamic pressures extracted at axial distances of $0.215R$ and $0.325R$ ($R = 0.914$ m) below the rotor disk exhibit strong agreement with the experimental data. This correlation verifies the solver's fidelity in accurately capturing highly unsteady rotor wake dynamics and slipstream effects.

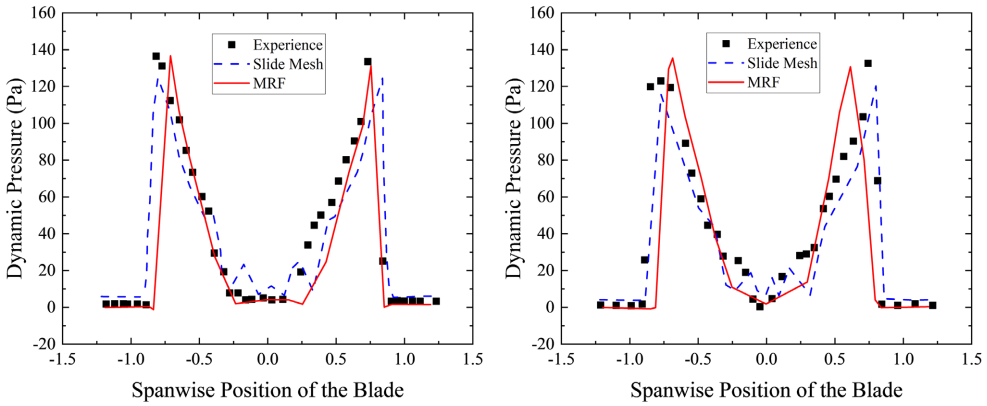

Figure 3. Dynamic Pressure at different positions below the rotor.

3.2. Validation of Coupled CFD/6-DOF Solver for Store Separation

To validate the coupled CFD/6-DOF solver for multi-body separation, the classic wing-store ejection benchmark [15] was simulated. Figure 4 depicts the computational domain and overset mesh topology.

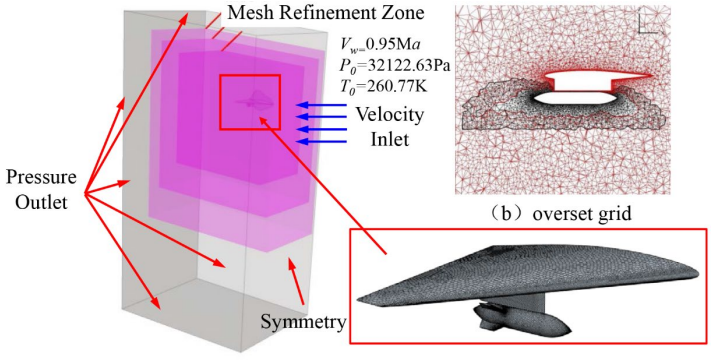

Figure 4. Example verification model and grid.

The store, initially suspended at a 0˚ angle of attack, was released under a predefined ejection force profile. All geometric, inertial, and ejection parameters strictly align as in [15].

As shown in Figure 5, the simulated time-histories of the three-axis velocities, displacements, angular rates, and attitude angles were compared with the corre-

sponding experimental data [15]. The highly consistent agreement demonstrates the robustness of the established methodology in resolving complex aerodynamic interference and trajectory propagation during dynamic separation.

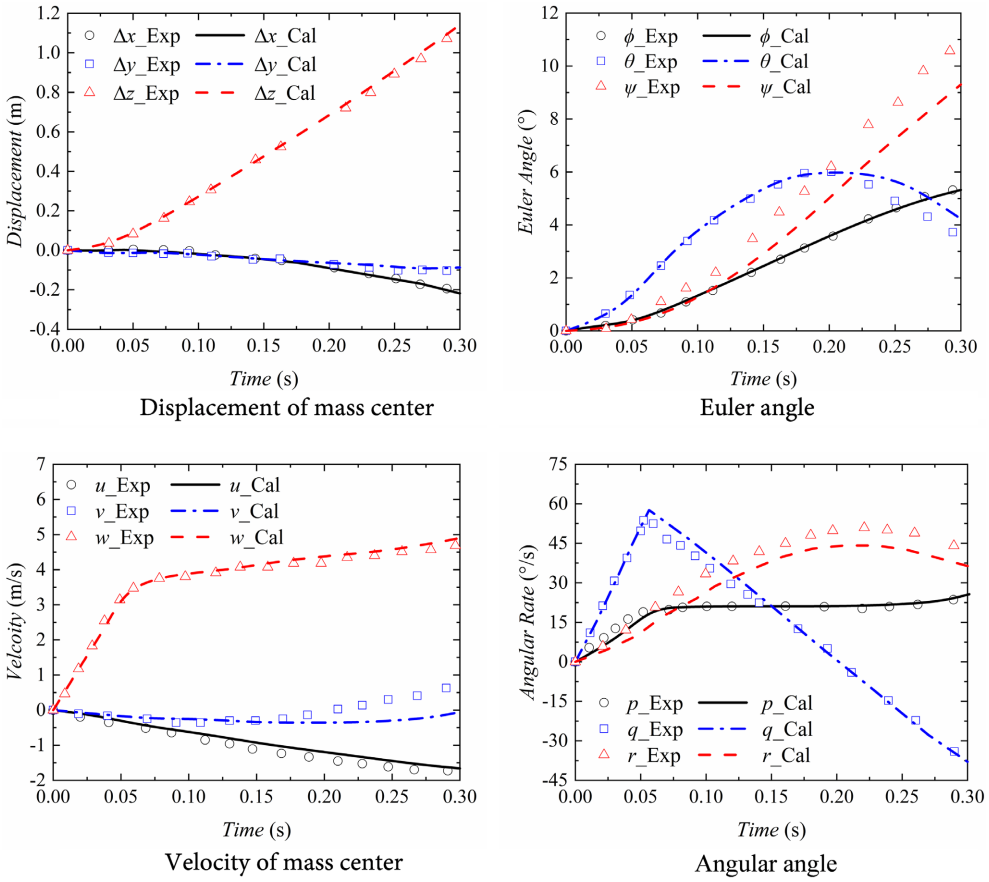

Figure 5. Trajectory and attitude variation curves of store separation.

4. Results and Analysis

This section characterizes the steady and unsteady aerodynamic interference acting on the sub-UAV upon release. To strictly isolate the aerodynamic effects, the 6-DOF kinematic responses are evaluated in a purely open-loop state. By comparing the raw, unmitigated disturbance moments against the sub-UAV's physical actuator limits, safe separation envelopes are established across distinct flight regimes, then determining the separation compatibility characteristics of the composite-wing carrier-store system.

4.1. Validation of coupled CFD/6-DOF Solver for Store Separation

To investigate the separation characteristics under fixed-wing flight conditions ($V_\infty = 42$ m/s), the sub-UAV was mounted inboard and outboard of the rotor booms at spanwise stations of $y = 650$ mm and $y = 1750$ mm, respectively.

As shown in **Figure 6**, the velocity contours with and without the installed sub-UAV. The flow-field topologies exhibit negligible variance across the mid-wing,

inboard, and outboard stations, implying that the resulting separation trajectories within these regions are kinematically equivalent.

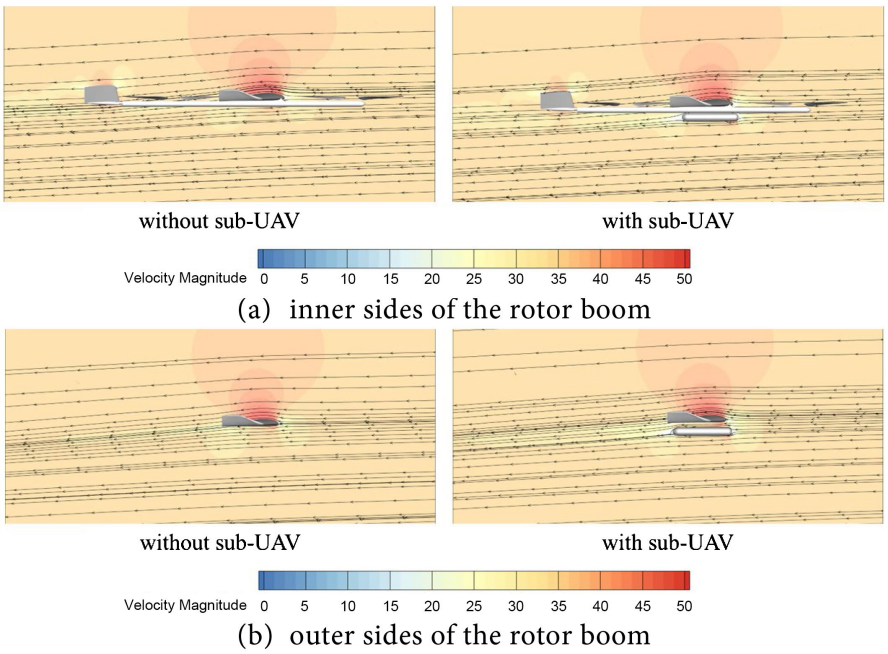

Figure 6. Velocity contour comparisons with and without the Sub-UAV.

To evaluate separation safety under fixed-wing cruise conditions, the Covert separation criterion was adopted: for slender external stores, the vertical drop distance must exceed a critical threshold—typically the maximum geometric radius of the store ($R_{\max}$)—within 0.25 s to ensure safe clearance. By expanding the longitudinal displacement via a Taylor series and retaining the first- and second-order terms corresponding to the initial relative velocity (Δ_1) and relative acceleration (Δ_2), as expressed in Equation (4) and Equation (5), the safe separation envelope is delineated in Figure 7. Consequently, both Regions A and B strictly satisfy the safety criteria.

$$\Delta z = \Delta_1 t + 0.5\Delta_2 t^2 \geq 0 \tag{4}$$

$$\Delta_1 = 1.8 - 0.125\Delta_2 \tag{5}$$

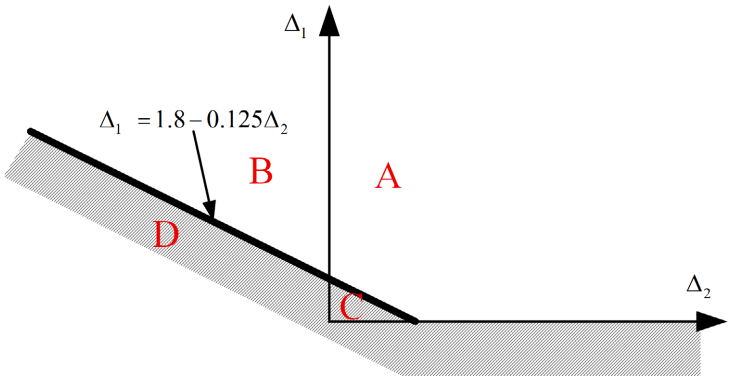

Figure 7. Safe separation regions in fixed-wing flight conditions.

Based on the WPFS standard model [15], the accelerated ejection force profile detailed in Table 3 was applied. Figure 8 illustrates the 6-DOF kinematic time-histories of the sub-UAV over the initial 0.4 s post-release window.

Table 3. The accelerated ejection force Table.

Point Location	Actuation Position (mm)	Ejection Force Vector (N)	Drag of aircraft (kN)
Sub-UAV CG Position	(2055, 1750, 20)	\	\
Front Ejection Point	(1955, 1750, 20)	(0, 0, 100)	(0, 0, 150)
Rear Ejection Point	(2155, 1750, 20)	(0, 0, 100)	(0, 0, 150)

The kinematic response demonstrates that the sub-UAV rapidly descends, achieving the critical safe separation clearance by $t = 0.16$ s, thereby satisfying the Covert criterion well ahead of the 0.25 s threshold. Throughout this deployment phase, both the relative vertical velocity (Δ_1) and acceleration (Δ_2) remain strictly positive, ensuring the separation trajectory is securely bounded within the established safe envelope (Region A). This dynamic behavior validates the prescribed ejection force parameters and definitively guarantees collision-free separation under fixed-wing cruise conditions.

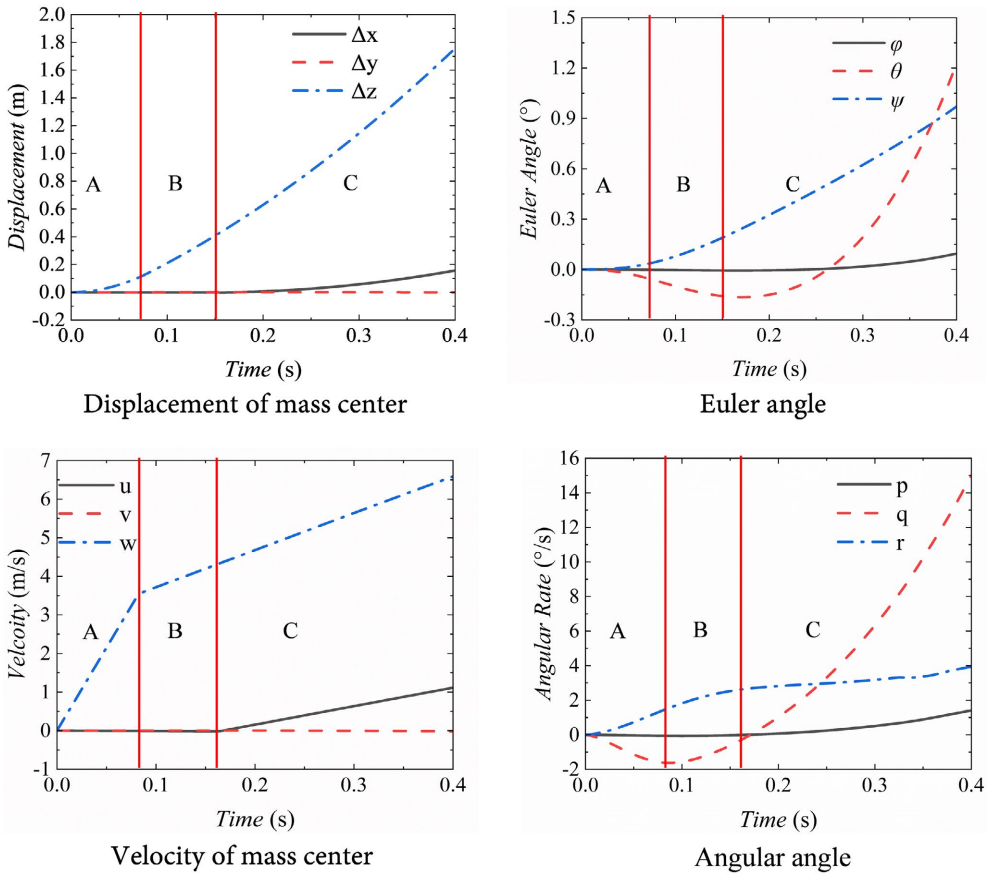

Figure 8. Trajectory and attitude variation curves of the sub-UAV during the separation process.

4.2. Separation Analysis in Hover Mode

Hover separation involves highly complex, nonlinear interactions among the rotor downwash, carrier wake, and sub-UAV airframe. To resolve these high-frequency vortex dynamics, the hover simulation was initialized at a 0 m/s freestream with a 3600 rpm rotor speed. The unsteady time step was strictly set to $\Delta t = 1 \times 10^{-4}$ s, utilizing up to 15 inner iterations per step to maintain residuals below 10^{-5}.

Flow Topology and Spatial Flow Distortion

The rotor downwash impinges upon the wing's upper surface, forming a high-pressure stagnation zone, while the lower surface is dominated by a severe counter-clockwise separation vortex (Region ① in Figure 9). This vortex imparts a catastrophic nose-down pitching moment on the sub-UAV.

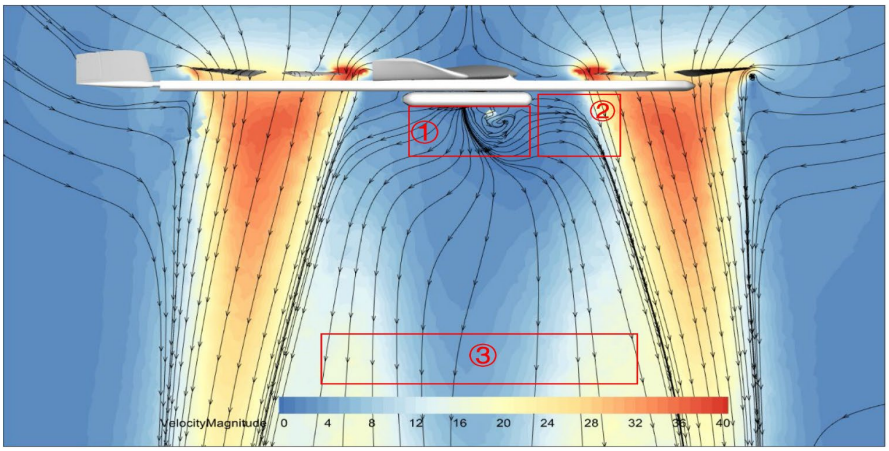

Figure 9. Velocity contours under the compound-wing in hover mode.

To quantify this spatial distortion, the sub-UAV was evaluated at five stations within the rotor-boom interference field (Figure 10): inboard of the rotor boom (Positions 1-3, corresponding to the outer disk, blade tip, and root), outboard of the boom (Position 4, mirroring the root), and a downstream wake-tracking point (Position 5, located 225 mm vertically below Position 3).

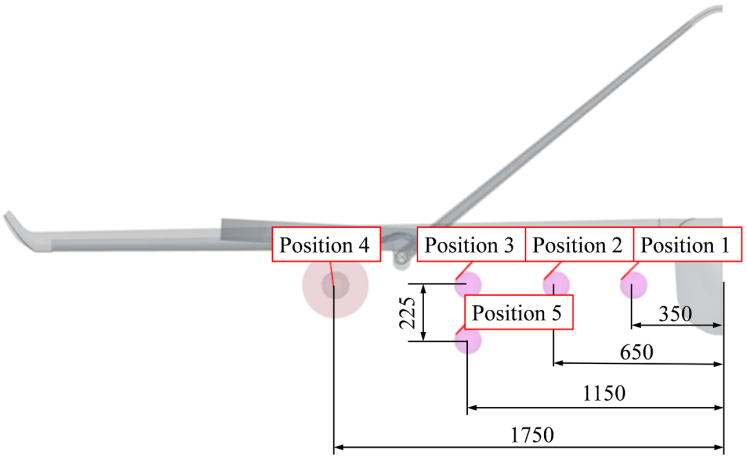

Figure 10. Velocity contours under the compound wing in hover mode.

In the subsequent velocity profiles (Figures 11-13), the initial CG of the sub-UAV is marked at $X = 2.055$ m, with shaded areas representing the rotor disk projections.

The induced velocity field exhibits extreme three-dimensional gradients. The vertical downwash (V_z) displays severe radial non-uniformity, accelerating from a −4 m/s tip upwash to a 37 m/s core downwash. This contracts into a high-shear "trumpet" shape that triggers violent roll-pitch oscillations. The lateral swirl (V_y) manifests as a 10 m/s side-wash, with its spatial gradient undergoing a sharp reversal near the hub (peaking at 40/s), severely jeopardizing directional stability.

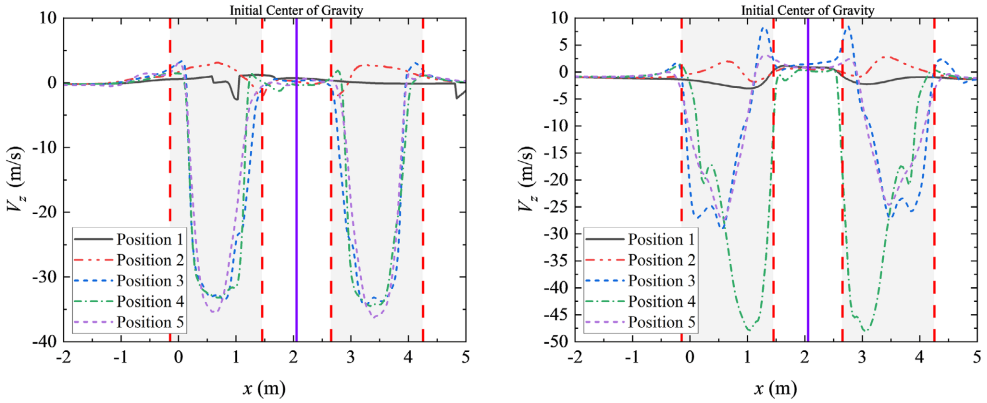

Figure 11. The spatial distribution of the Vertical induced velocity at different positions.

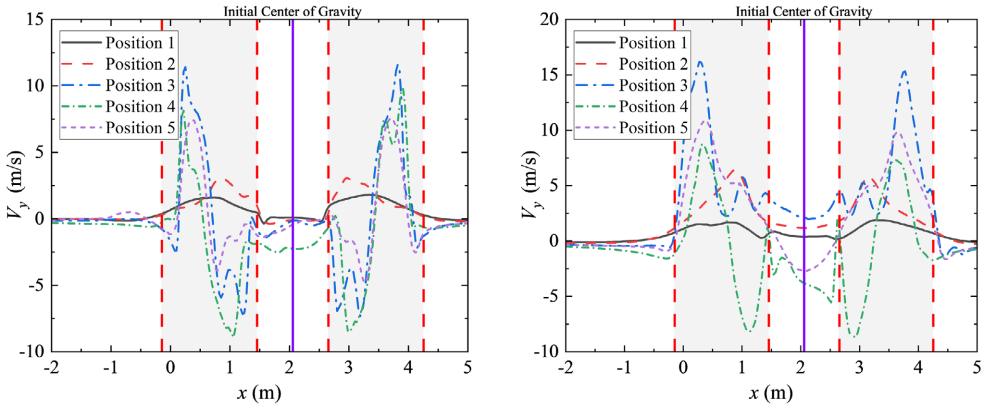

Figure 12. The spatial distribution of the Lateral induced velocity at different positions.

Concurrently, the longitudinal flow (V_x, fluctuating between −8 m/s and +10 m/s) accelerates outboard of the blunt rotor boom while stagnating inboard, generating localized pulsations that decay into far-field turbulence.

As can be seen from Figures 11-13, the introduction of the 3˚ inboard cant angle causes the overall streamlines to tilt outward, resulting in an approximately 13% reduction in downwash velocity at the inboard section (Position 3), while the downwash velocity at the outboard section opposite to the cant direction (Position

4) increases by around 30%; meanwhile, the amplitude of the lateral induced velocity rises by about 10% at the inboard side, whereas the longitudinal induced velocity shows an approximately 70% increase in amplitude at the outboard section (Position 4) and a roughly 23% decrease at the inboard section (Position 3).

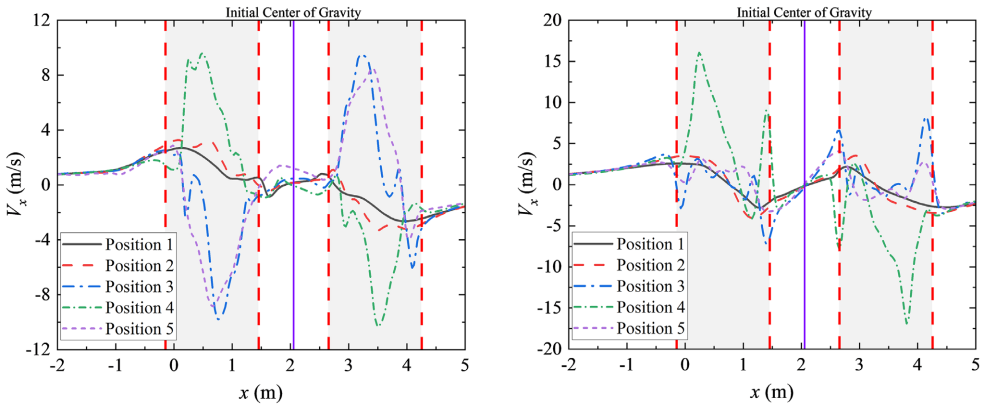

Without inboard cant angle　　With inboard cant angle

Figure 13. The spatial distribution of the Longitudinal induced velocity at different positions.

To translate these non-linear gradients into actionable safety boundaries, the aerodynamic moments are evaluated using a quasi-steady surrogate model. Assuming the perturbing moments are dominated by the dynamic pressure differential between the nose and tail sections, the induced pitching (M_y) and yawing (M_z) moments are formulated as:

$$M_y = \frac{1}{2}\rho\left(\bar{l}_{\text{nose}}V_{z,\text{nose}}^2 - \bar{l}_{\text{tail}}V_{z,\text{tail}}^2\right)S_{\text{ref}} \tag{6}$$

$$M_z = \frac{1}{2}\rho\left(\bar{l}_{\text{tail}}V_{y,\text{tail}}^2 - \bar{l}_{\text{nose}}V_{y,\text{nose}}^2\right)S_{\text{ref}} \tag{7}$$

where $V_{z,\text{nose}}$ and $V_{z,\text{tail}}$ denote the local vertical induced velocities at the nose and tail point of the sub-UAV, respectively; $V_{y,\text{nose}}$ and $V_{y,\text{tail}}$ are the corresponding lateral induced velocities; ρ is the air density; S_{ref} is the reference area of the sub-UAV; and l_{nose} and l_{tail} represent the longitudinal moment arms from the CG to the nose and tail point of the sub-UAV.

To establish a rigorous safety criterion, both theoretical aerodynamic authority and physical hardware constraints were evaluated. Based on empirical sizing [16], applying horizontal and vertical tail volume coefficients of 0.7 and 0.04, along with elevator and rudder area ratios of 35% and 20%, geometrically establishes a 2:1 pitch-to-yaw control authority ratio. Furthermore, assuming a full-deflection $\Delta C_L \approx 0.4$ for the tandem-wing [17], the theoretical maximum aerodynamic restorative moment reaches 12.54 N·m.

However, typical commercial micro-servos are mechanically bottlenecked by a stall torque of approximately 40 kg·cm (4 N·m). Imposing this hardware limit alongside the inherent 2:1 geometric ratio explicitly bounds the absolute actuator saturation limits at 4 N·m for pitch and 2 N·m for yaw. Exceeding these mechanical

thresholds inevitably causes actuator stall and catastrophic attitude divergence.

By mapping the calculated moments across the interference field (Figure 14 and Figure 15), the safe separation envelope is strictly defined as the spatial region satisfying:

$$|M_y| \leq 4\ \mathrm{N\cdot m}, \quad |M_z| \leq 2\ \mathrm{N\cdot m} \tag{8}$$

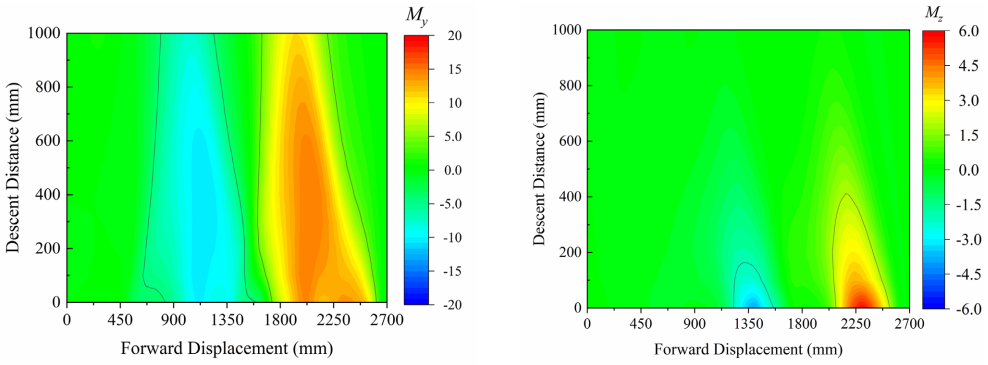

Figure 14. Safe separation envelope in position 3.

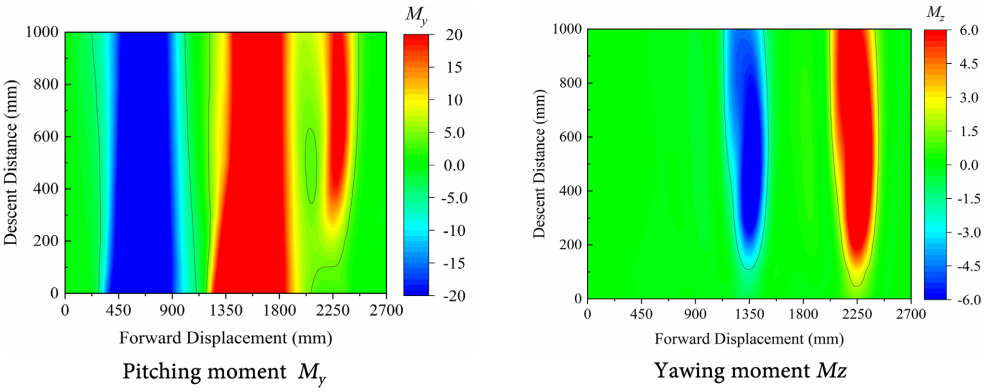

Figure 15. Safe separation envelope in position 4.

Regions exceeding these mathematical thresholds are strictly identified as actuator saturation zones. Within these bounds, the non-linear rotor interference completely overpowers the sub-UAV's available control authority, inevitably triggering catastrophic attitude divergence.

Focusing on the initial 1000 mm descent phase, quantitative comparison of the moment envelopes (Figure 14 and Figure 15) reveals a significant spatial asymmetry between inboard and outboard stations, which is fundamentally driven by the 3˚ inboard cant angle of the carrier rotors. This geometric tilt deflects the high-energy slipstream and its associated tip vortices toward the fuselage, intensifying aerodynamic impingement on the outboard section of the rotor boom. As a result, the outboard station (Position 4) experiences sustained control surface saturation, with induced pitching moments consistently exceeding the 4 N·m limit throughout the entire 1000 mm vertical descent. Based on the estimated proportional dif-

ference of downwash increment between the inboard and outboard sides, the introduction of the 3˚ inboard cant angle increases the amplitude difference of control moment between the inboard and outboard stations by a factor of approximately 1.96, which is consistent with the color amplitude of the safe separation envelopes for Position 3 and Position 4. Estimated from the boundary distance along the forward flight direction, the overall envelope of Position 4 shifts forward after the value increases, with the first failure envelope expanded by 10%; the upstream range of the second failure envelope remains basically unchanged, while its downstream range is expanded by 30%. In contrast, the inboard station (Position 3) lies in a relatively shielded wake environment, where flow interference decays rapidly beyond a 600 mm vertical clearance, leaving a narrow yet viable safety window. These findings confirm that the 3˚ rotor cant angle acts as an aerodynamic "disturbance magnifier" for outboard hardpoints, thus mandating an inboard-weighted deployment strategy to ensure controllable release.

4.3. Comparison of Separation Strategies

To establish the optimal separation protocol, three deployment strategies were evaluated:

1) Tube-launch (600 N thrust) at the inboard station (Position 3);
2) Tube-launch (600 N thrust) at the outboard station (Position 4);
3) Accelerated Gravity-drop and launch with low thrust (30 N) at Position 4;
4) Accelerated Gravity-drop with launch with high thrust (600 N) at Position 4.

4.3.1. Tube-Launch Separation Strategies

Although tube-launch systems impart a high initial velocity, the sub-UAV experiences severe unsteady pitch oscillations upon exiting the tube (Figure 16).

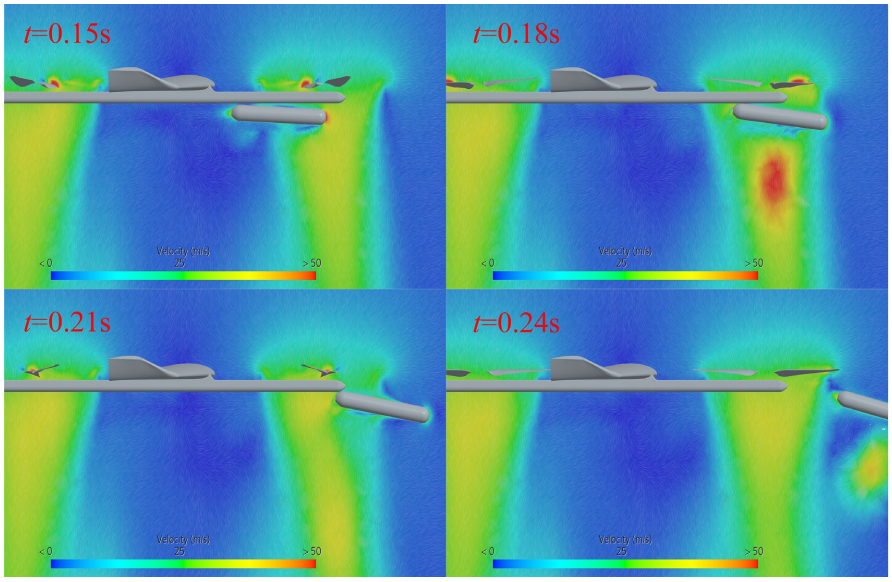

Figure 16. Velocity Contours and attitude variation of the sub-UAV during the separation process.

This instability is primarily driven by the aerodynamic lag effect: as the vehicle rapidly pierces the intense shear layer, the local pressure field fails to equilibrate instantaneously, resulting in a delayed but severe pitch-up moment once the sub-UAV clears the wake. This phenomenon aligns with the flow history effect documented by Lijewski [10].

Critically, if this tube-launch were deployed at the outboard station (Position 4), the 3˚ rotor cant angle would focus the high-energy slipstream directly onto the trajectory, amplifying the local shear gradient. Under such extreme spatial interference, the induced unsteady moments would drastically overpower the actuators, inevitably causing rapid attitude divergence. Consequently, while tube-launching is viable during fixed-wing cruise, its inherent coupling with aerodynamic lag makes it kinematically incompatible with the severe VTOL hover environment.

4.3.2. Accelerated Gravity-Drop Separation Strategies

A comparative analysis of the vorticity evolution (visualized via Q-criterion contours at $Q = 1000\ \mathrm{s}^{-2}$) was conducted between the 600 N and 30 N thrust profiles in Figure 17 and Figure 18.

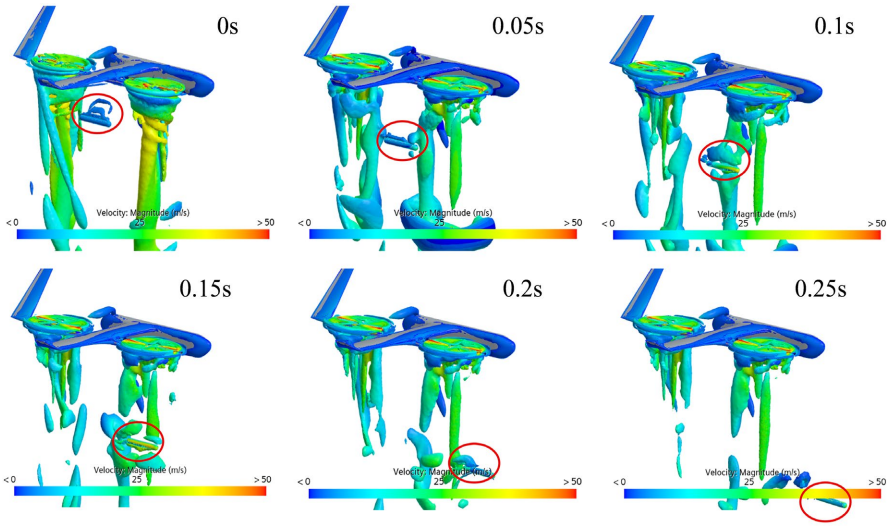

Figure 17. Q-criterion contours at 600 N accelerated scheme.

Under the 600 N accelerated scheme (Figure 17), the sub-UAV demonstrates rapid kinematic penetration. Between $t = 0.1$ s and 0.25 s, the descending fuselage acts as an aerodynamic wedge, injecting massive localized momentum into the rotor's tip vortices. This intense perturbation forcibly disrupts the spatial coherence of the helical wake topology. The pristine vortex rings are rapidly fragmented into disorganized, small-scale structures. This forced "vortex breakdown" mechanism drastically accelerates viscous dissipation, thereby shortening the sub-UAV's residence time within the severe interference zone and strictly limiting the maximum altitude drop to 2.3 m.

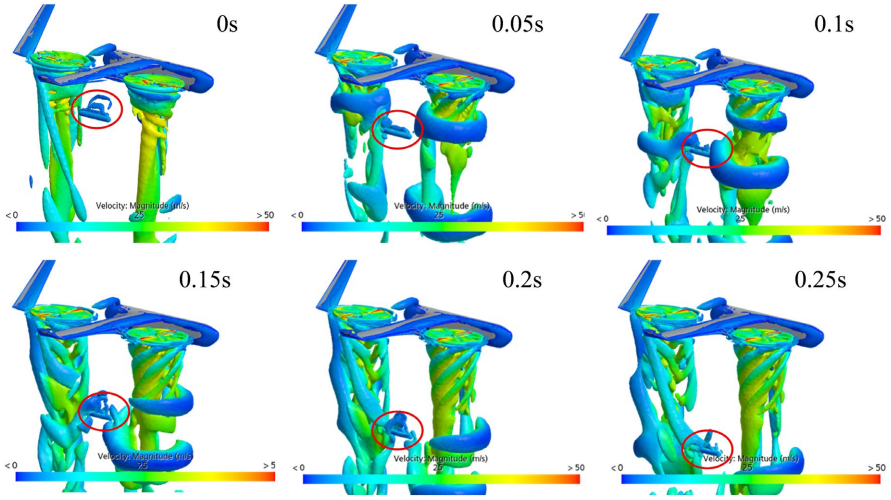

Figure 18. Q-criterion contours at 30 N accelerated scheme.

Conversely, under the 30 N scheme (Figure 18), insufficient vertical momentum causes the sub-UAV to stagnate within the intense shear layer. Lacking the kinetic energy required to sever the main vortex structures, the vehicle acts merely as a blunt obstacle. Consequently, the helical vortices maintain high structural coherence, continuously enveloping and impinging upon the fuselage. This prolonged vortex-body coupling converts the flow's kinetic energy into sustained, unbalanced aerodynamic moments, ultimately leading to an unrecoverable altitude loss of 8.35 m.

4.3.3. Comparison between the Quasi-Steady Envelope Predictions and the Coupled URANS/6-DOF

The actual pitching moment envelopes during the deployment process with real rotor blade rotation can be seen in Figure 19 and Figure 20. Figure 19(a) is the steady-state prediction envelope described above, Figure 19(b) is the unsteady envelope at 0.1 s post-deployment (with the black line showing the actual trajectory of the 600 N accelerated scheme), and Figure 20 presents the monitored pitching moment time-history during deployment.

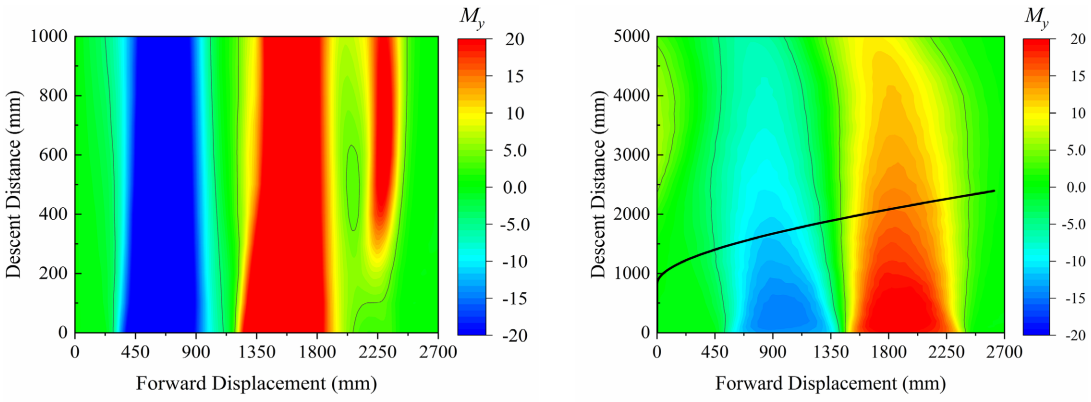

(a) Quasi-steady Pitching moment M_y predction envelope

(b) Unsteady Pitching moment M_y prediction at 0.1 s and the real envelope

Figure 19. Comparison between the quasi-steady envelope predictions and the unsteady one in position 4.

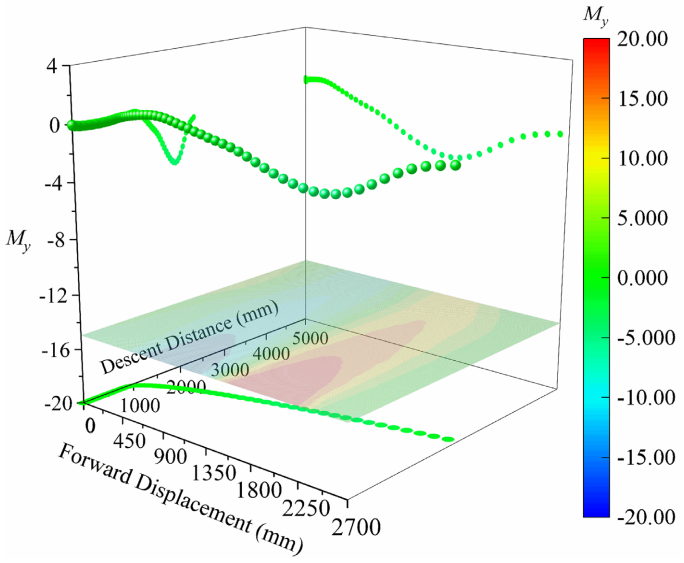

Figure 20. Comparison envelope predictions and the real Pitching moment envelope at 600 N accelerated scheme in position 4.

The quasi-steady envelope is notably more conservative than the unsteady one, and neither envelope considers the time effect on the sub-UAV's motion state. The actual pitching moment is continuous with clear time dependence, varying within 4 Nm with almost no actuator saturation. This indicates that the full-coupled simulation combining unsteady calculation and 6-DOF dynamics yields a safer separation assessment. The quasi-steady calculation yields a more stringent safety boundary than the actual simulation: any condition that meets the quasi-steady safety requirements will definitely satisfy the unsteady safety criteria, so quasi-steady calculation can be used as a more conservative prediction scheme.

5. Conclusions

This study systematically investigates the non-linear aerodynamic interference and separation safety of a composite-wing UAV in hover mode. By integrating quasi-steady spatial envelope modeling with transient URANS simulations, the dynamic mechanisms of rotor-wing-body coupling are elucidated. The principal conclusions are as follows:

1) Intense Spatial Heterogeneity and Geometric Amplification: The rotor slipstream dictates an extreme interference environment, characterized by a 37 m/s core downwash and a 40/s lateral shear gradient. Critically, the 3° inboard rotor cant angle acts as an aerodynamic disturbance magnifier; it skews the wake trajectory inboard, causing catastrophic actuator saturation (consistently exceeding the 4 N·m pitch limit) at the outboard stations. Consequently, inboard hardpoint placement is strictly mandated for this configuration.

2) The Conservative Value of Quasi-Steady Envelopes: The formulated quasi-steady surrogate model, based on unperturbed flow-field pressure differentials (M_y, M_z), inherently overestimates dynamic aerodynamic loads. However, due

to its structural conservatism and computational efficiency, this methodology remains highly valuable. It serves as an indispensable tool for rapidly delineating preliminary safe separation boundaries and ensuring baseline aerodynamic compatibility during the conceptual design phase.

3) Dynamic Relief via Forced Vortex Breakdown: Transient simulations reveal a fundamental physical divergence from quasi-steady assumptions. Under a high-thrust (600 N) deployment, the sub-UAV exhibits a pronounced "aerodynamic wedge effect." The massive localized momentum injection actively severs and shatters the coherent toroidal vortices of the rotor wake. This forced vortex breakdown accelerates viscous dissipation, effectively relieving local pressure gradients and preventing the continuous vortex-body coupling observed in low-momentum (30 N) stagnation drops.

4) Optimized Deployment Strategy: Traditional tube-launch methods are kinematically incompatible with the hover mode due to violent, unrecoverable attitude divergence induced by the aerodynamic lag effect upon piercing the shear layer. Instead, the "accelerated gravity-drop" strategy is established as the optimal solution. By utilizing active downward thrust to ensure rapid slipstream penetration, this strategy minimizes residence time within the severe interference zone, thereby guaranteeing superior attitude stability in complex low-altitude VTOL environments.

Funding

Graduate Student Innovation Special Fund Project of 2024: Aerodynamic Characteristics Study on the Deployment Process of Tandem-Wing UAV Delivery (Fund Number: YC2024-030).

Conflicts of Interest

The authors declare no conflicts of interest regarding the publication of this paper.

References

[1] Yang, L. (2018) Study on the Dynamic Problems of Air-Launch in Separation Process. Ph.D. Thesis, Northwestern Polytechnical University. (In Chinese)

[2] Lu, Y., Chen, Q., Wang, P., *et al.* (2023) Design and Experiment of a Small Air-Launched UAV. *Acta Aeronautica et Astronautica Sinica*, 44, Article ID: 528642. (In Chinese)

[3] Zhang, H. (2021) Multidisciplinary Design Optimization for Conceptual Design of Electric Quadrotor Fixed-Wing Hybrid Unmanned Air Vehicle. Ph.D. Thesis, Northwestern Polytechnical University. (In Chinese)

[4] Leishman, J.G. (2006) Principles of Helicopter Aerodynamics. Cambridge University Press.

[5] Wang, F., Liu, B., Lu, W., Wang, Z., Xiong, C. and Song, Y. (2026) Research on Controllable Stage-Separation Testing Technology for Hypersonic Multi-Body Vehicles. *Chinese Journal of Theoretical and Applied Mechanics*, **58**, 318-328. (In Chinese)

[6] Goerttler, A. and Schnepf, C. (2024) Numerical Investigation of an Unmanned Aerial

Vehicle Launch from Military Transport Aircrafts. *Journal of Aircraft*, **61**, 695-708. https://doi.org/10.2514/1.c037360

[7] Zhao, W.Q., Zhao, G.Q., Cao, C.K. and Zhao, Q.J. (2025) Analysis of Motion Characteristics of Helicopter Mounted UAVs during the Deployment. *Flight Dynamic*, No. 4, 41-46, 61. (In Chinese)

[8] Li, H., Cui, P.C., Jia, H.Y., Tang, J., Zhang, J., Gong, X.Q., *et al*. (2025) Numerical Simulation Method and Application of Aircraft Multi-Body Separation. *Advances in Mechanics*, **55**, 497-540. (In Chinese)

[9] Wolf, C.C., Schanz, D., Schwarz, C., Heintz, A., Bosbach, J., Strübing, T., *et al*. (2024) Volumetric Wake Investigation of a Free-Flying Quadcopter Using Shake-The-Box Lagrangian Particle Tracking. *Experiments in Fluids*, **65**, Article No. 152. https://doi.org/10.1007/s00348-024-03880-3

[10] Lijewski, L.E. and Suhs, N.E. (1994) Time-accurate Computational Fluid Dynamics Approach to Transonic Store Separation Trajectory Prediction. *Journal of Aircraft*, **31**, 886-891. https://doi.org/10.2514/3.46575

[11] Gao, L. (2020) Research on Design and Control of Catapult Launched Tandem-Wing Flying Robot with Variable Sweep. Ph.D. Thesis, Harbin Institute of Technology. (In Chinese)

[12] Cheng, Y., Zhou, Z. and Wang, Z. (2022) Research on Deployment Process of Gravitational Airdrop UAV. *Journal of Northwestern Polytechnical University*, **40**, 485-492. https://doi.org/10.1051/jnwpu/20224030485

[13] Yan, X.X., Niu, J.P., Xu, Y.T. and Li, C.W. (2024) Numerical Research on Store Separation Based on Polyhedral Overset Mesh. *Physics of Gases*, **9**, 36-44. (In Chinese)

[14] Mckee, J. and Naeseth, R. (1958) Experimental Investigation of the Drag of Horizontal Plates and Cylinders in the Slipstream of a Hovering Rotor. NACA-TN-4239.

[15] Heim, E.R. (1991) CFD Wing/Pylon/Finned Store Mutual Interference Wind Tunnel Experiment. AEDC-TSR-91 P4.

[16] Raymer, D. (2018) Aircraft Design: A Conceptual Approach, Sixth Edition. American Institute of Aeronautics and Astronautics, Inc. https://doi.org/10.2514/4.104909

[17] Kryvokhatko, I.S. (2019) Tandem-Scheme Aircraft Controllability. 2019 *IEEE 5th International Conference Actual Problems of Unmanned Aerial Vehicles Developments* (*APUAVD*), Kiev, 22-24 October 2019, 149-152. https://doi.org/10.1109/apuavd47061.2019.8943843